Draft version May 18, 2022
Typeset using LaTeX **preprint2** style in AASTeX62

Nucleosynthesis Constraints on the Explosion Mechanism for Type Ia Supernovae

Kanji Mori,[1,2] Michael A. Famiano,[3,2] Toshitaka Kajino,[4,2,1] Toshio Suzuki,[5,2] Peter M. Garnavich,[6] Grant J. Mathews,[6,2] Roland Diehl,[7,2] Shing-Chi Leung,[8] and Ken'ichi Nomoto[8]

[1] *Graduate School of Science, The University of Tokyo, 7-3-1 Hongo, Bunkyo-ku, Tokyo, 113-0033 Japan*
[2] *National Astronomical Observatory of Japan 2-21-1 Osawa, Mitaka, Tokyo, 181-8588 Japan*
[3] *Department of Physics, Western Michigan University, Kalamazoo, Michigan 49008 USA*
[4] *School of Physics and Nuclear Energy Engineering, and Internationsl Research Center for Big-Bang Cosmology and Element Genesis, Beihang University, Beijing 100083, P.R. China*
[5] *Department of Physics, College of Humanities and Sciences, Nihon University 3-25-40 Sakurajosui, Setagaya-ku, Tokyo 156-8550 Japan*
[6] *Departmant of Physics, Center for Astrophysics, University of Notre Dame, Notre Dame, IN 46556, USA*
[7] *Max Planck Institut für extraterrestrische Physik, D-85748 Garching, Germany*
[8] *Kavli Institute for the Physics and Mathematics of the Universe (WPI), The University of Tokyo, Kashiwa, Chiba 277-8583, Japan*

ABSTRACT

Observations of type Ia supernovae include information about the characteristic nucleosynthesis associated with these thermonuclear explosions. We consider observational constraints from iron-group elemental and isotopic ratios, to compare with various models obtained with the most-realistic recent treatment of electron captures. The nucleosynthesis is sensitive to the highest white-dwarf central densities. Hence, nucleosynthesis yields can distinguish high-density Chandrasekhar-mass models from lower-density burning models such as white-dwarf mergers. We discuss new results of post-processing nucleosynthesis for two spherical models (deflagration and/or delayed detonation models) based upon new electron capture rates. We also consider cylindrical and 3D explosion models (including deflagration, delayed-detonation, or a violent merger model). Although there are uncertainties in the observational constraints, we identify some trends in observations and the models. We make a new comparison of the models with elemental and isotopic ratios from five observed supernovae and three supernova remnants. We find that the models and data tend to fall into two groups. In one group low-density cores such as in a 3D merger model are slightly more consistent with the nucleosynthesis data, while the other group is slightly better identified with higher-density cores such as in single-degenerate 1D-3D deflagration models. Hence, we postulate that both types of environments appear to contribute nearly equally to observed SNIa. We also note that observational constraints on the yields of ^{54}Cr and ^{54}Fe, if available, might be used as a means to clarify the degree of geometrical symmetry of SNIa explosions.

kanji.mori@nao.ac.jp

Keywords: white dwarfs — nucleosynthesis — supernovae: general — nuclear reactions

1. INTRODUCTION

Type Ia supernovae (SNIa) are thought to result from accreting CO or white dwarfs (WDs) in close binaries (e.g., Hoyle & Fowler 1960; Arnett 1996; Hillebrandt & Niemeyer 2000; Boyd 2008; Illiadis 2008). For sufficiently high central densities, the initiation of carbon, oxygen, and/or neon thermonuclear burning in the core can result in a violent explosion that disrupts the entire star. The subsequent nucleosynthesis can result in an abundance of Fe-peak elements. The ejection of these elements into the interstellar medium (ISM) contributes to the galactic chemical enrichment. Moreover, a carefully-selected subset of SNIa are currently employed as standard candles in cosmology to measure the acceleration of the Universe (Riess et al. 1998; Perlmutter et al. 1999; Schmidt et al. 2008).

Despite their importance in Fe-peak enrichment in the ISM, the origin of SNe Ia, including the progenitors and the actual explosion mechanism is still a subject of debate (e.g., Maoz, Mannucci, & Nelemans 2014; Hillebrandt & Niemeyer 2000; Nomoto, Iwamoto, & Suzuki 1995). Two major progenitor models have been hypothesized. One case involves accretion from a non-degenerate companion. The WD mass then approaches the Chandrasekhar mass inducing a SN Ia. This is known as the single-degenerate progenitor model and the accreting WD is dubbed a "Chandra model" star because its mass approaches the Chandrasekhar mass. The other case is the double-degenerate model. This case involves two sub-Chandrasekhar-mass WDs ("sub-Chandra") that merge to form a SN Ia (Iben & Tutukov 1984; Webbink 1984). Several violent merger (VM) models (e.g., Pakmor et al. 2013; Sato et al. 2016) have attempted to simulate these explosive events.

The Chandra and sub-Chandra models involve different central densities ρ_c of the white dwarf at the time of central ignition. In the Chandra model, $\rho_c > 10^9$ g cm^{-3}, while $\rho_c \lesssim 10^8$ g cm^{-3} in the sub-Chandra models (Wang & Han 2012; Nomoto, Kamiya, & Nakasato 2013). This changes the explosion dynamics of the subsequent supernova. For Chandra models, the thermonuclear burning propagates outward as a subsonic flame front known as a deflagration wave (Nomoto, Sugimoto, & Neo 1976; Nomoto, Thielemann, & Yokoi 1984). Burning is expected to be enhanced by an increase in the surface area from Rayleigh-Taylor instabilities at the front (Müller & Arnett 1982; Arnett & Livne 1994; Khokhlov 1995). This front may undergo a deflagration-to-detonation transition (DDT: Blinnikov & Khokhlov 1986; Khokhlov 1991; Iwamoto et al. 1999) for a strong enough deflagration. This type of explosion dynamics has been modeled in 3D simulations (e.g., Gamezo, Khokhlov, & Oran 2005; Röpke et al. 2006; Seitenzahl et al. 2013a).

The explosion mechanism of SNe Ia is also related to its nucleosynthesis. The results of this nucleosynthesis may be inferred from direct light-curve observations and/or spectral observations of the remnants. Indeed, the decays of ^{56}Ni and its daughter ^{56}Co are the primary power source of the light-curves (Arnett 1979).

For a sufficiently high central density the Fermi energy of the electrons can exceed the energy threshold for electron capture (EC) reactions on ambient nuclei. An increase in the EC rates in the subsequent nucleosynthesis, can reduce the overall electron fraction Y_e, defined as the sum over all nuclear species:

$$Y_e \equiv \sum_i Z_i Y_i, \tag{1}$$

where Y_i is the abundance of a given species with proton number Z_i. Thus, the larger central densities associated with the Chandra models are expected to result in a shift to lower electron fraction and a shift of the nucleosynthesis toward more neutron-rich nuclei as compared to the sub-Chandra models. However, this may be influenced by a variety of features in the models such as the flame speed, convection, and rotation of the system (Benvenuto et al. 2015).

The new aspects of the present work are to make revised nucleosynthesis calculations based upon new EC rates. We also make a new summary of the nucleosynthesis products in several recently observed light curves.

In this paper we have selected observational constraints for the purpose of comparing specific nucleosynthesis predictions of SNIa models. Toward that aim we make use of our recently updated nucleosynthesis treatment concerning the weak reaction rates involved in electron captures and the resulting change in Y_e. The important roles of nuclear e-capture rates on pf-shell nuclei for the synthesis of iron-group elements in SN Ia explosions have been discussed in (Langanke & Martínez-Pinedo 2003), where the KBF and KB3G shell-model Hamiltonians were used. However, new e-capture rates have been obtained by (Honma & Suzuki 2017) with a new pf-shell Hamiltonian, GXPF1J, which can better describe the Gamow-Teller (GT) strengths in Ni and Fe isotopes. Especially in ^{56}Ni, the GXPF1J can reproduce the experimental GT data very well in contrast to the KB3G and KBF. A comparison of the GT strengths and e-capture rates in ^{56}Ni and ^{54}Fe as well as the impact of the new rates on elemental abundances in SN Ia explosions are discussed in detail in (Mori et al. 2016).

Therefore, in this paper we concentrate on iron group elemental and isotopic ratios as observational constraints. We then discuss a number of selected models intended to address the range of nucleosynthesis conditions relevant to those iron group elements and isotopes. We include both Chandra- and sub-Chandra-models here, and also consider 1D, 2D, and 3D simulations. In this way we can test whether the assumed symmetry of the models or the type of explosion mechanism are the main features characterizing the resultant nucleosynthesis.

We find that the models and observed nucleosynthesis tend divide into two nearly equally favored groups roughly characterized by the central densities during thermonuclear burning. One set of data is consistent with the low central densities of sub-Chandra merger models, while the other favors the higher central densities of Chandra models. We also speculate on which future observables might help to distinguish the degree of symmetry in these explosions.

Section 2 presents the observational constraints that we have selected for our comparisons among models. Section 3 presents the available models covering the space of hypothetical nucleosynthesis conditions. In Section 4 we compare various models both with each other and with the observational constraints. Section 5 presents the conclusions and provides suggestions for future work.

2. OBSERVATIONAL CONSTRAINTS

Supernova light curves and their spectral evolution have been observed for many events and have been frequently discussed in the context of theoretical models (see, e.g., Höflich et al. 2017). Here, we select observations of recent years, from which key nucleosynthesis results are extracted to compare to nucleosynthesis results in the models. Observations mainly focus on

(1) The late-time light curve evolution and its inferred energy source.

(2) Supernova-remnant abundances for iron group elements including Mn.

(3) Direct γ-ray measurements of the ejected mass of ^{56}Ni.

(4) A comparison to solar abundances, specifically for Mn.

A summary of the observational data employed in the present study is summarized in Table 1.

2.1. *Light-curve analysis*

The usefulness of the late-time light-curve analysis with respect to the presence or absence of longer-lived radioactive energy sources has been demonstrated for SN1987A (Fransson & Kozma 2002), and was discussed by Seitenzahl et al. (2009) in the context of various isotopes such as ^{55}Fe. It has also been pointed out that charactaristic X-rays from long-lived nuclei can be used to study supernova nucleosynthesis (Leising 2001).

Recently, key results have been added for SN 2011fe (Shappee et al. 2017), SN 2012cg (Graur et al. 2016), SN 2014J (Yang et al. 2018), SN 2015F Graur et al. (2018), and SN 2013aa (Jacobson-Galán et al. 2018). Shappee et al. (2017) used HST and the Large Binocular Telescope to follow the light curve of nearby SN2011fe for an unprecedented time of 1840 days. In particular, they tested for the decays of ^{57}Co$\rightarrow^{57}$Fe ($t_{1/2} = 271.79$ d) and ^{55}Fe$\rightarrow^{55}$Mn ($t_{1/2} = 999.67$ d). The late-time light curve of SN 2011fe is fit significantly better if the radioactive-energy input from ^{57}Co and ^{55}Fe are included. Their best fit was for abundance ratios of ^{57}Co/^{56}Ni = 0.03, and ^{55}Fe/^{57}Co = 0.07. The fit is also acceptable without the contribution from ^{55}Fe. Hence, they only provide a 2σ upper limit of ^{55}Fe/^{57}Co $\leq$ 0.22. Nevertheless, this inferred abundnace of ^{57}Co is consistent with the direct detection of γ-rays from ^{57}Co in SN 1987A (Kurfess et al. 1992). We use their estimate for SN2011fe of $\log(^{57}\mathrm{Co}/^{56}\mathrm{Ni}) = -1.59^{+0.06}_{-0.07}$.

A recent late-time (day 1034) spectrum of SN2011fe (Taubenberger et al. 2015) supports this indirectly: Fransson & Jerkstrand (2015) find the need for energy injection by ^{57}Co. Also, from the observed flux level in their spectrum they require a production ratio of ^{57}Ni/^{56}Ni of 2.8 times the solar ratio. Shappee et al. (2017) concluded that a violent merger model is favored for SN2011fe because it produces a ^{55}Fe/^{57}Co ratio of 0.27, which is in better agreement with the observational limit. However, it should be noted that the estimated isotopic ratio is subject to systematic uncertainties due to a lack of detailed knowledge on the physical processes including electron/positron escape and light echoes (Kerzendorf et al. 2017; Dimitriadis et al. 2017).

Graur et al. (2016) also used HST to track the light curve of SN 2012cg out to 1055 days. They determined the slope of the light curve decay at early times when ^{56}Co decay powers the light curve and the supernova should already be transparent to gamma rays. They then extrapolated to times beyond day 500 to find that they needed another source of energy. A blue excess that had been reported in the early light curve of SN 2012cg could be interpreted as evidence for an interaction between the supernova ejecta and a non-degenerate companion (Marion et al. 2016). This interpretation is debated by Shappee et al. (2018) from a re-analysis of these data. Nevertheless, contamination by the light echo cannot be excluded (Graur et al. 2016).

From these considerations, Graur et al. (2016) estimated a mass ratio ^{57}Co/^{56}Co of $0.043^{+0.012}_{-0.011}$ or $\log(^{57}\mathrm{Co}/^{56}\mathrm{Ni}) = -1.36^{+0.11}_{-0.13}$. This is somewhat higher than the ratio determined for SN 2011fe. But we note that such constraints are indirect, and depend upon assumptions about how the light-curve evolution is driven by those radioactive species.

In similar ways, the ^{57}Co/^{56}Ni ratio has been estimated for SN 2014J, 2015F, and 2013aa using HST. Yang et al. (2018) observed late light curves of SN 2014J to 1181 days and esti-

Table 1. Observations

	SN 2011fe [1]	SN 2012cg [2]	SN 2014J [3,4]	SN 2015F [5]	SN 2013aa [6]	SNR 3C 397 [7]	Kepler [7]	Tycho [7]	Solar [8]
$\log_{10}(^{57}\mathrm{Co}/^{56}\mathrm{Ni})$	$-1.59^{+0.06}_{-0.07}$	$-1.36^{+0.11}_{-0.13}$	$-1.18^{+0.06}_{-0.05}$	$-2.40^{+0.25}_{-0.30}$	$-1.70^{+0.18}_{-\infty}$				
$\log_{10}(^{55}\mathrm{Fe}/^{57}\mathrm{Co})$	$-1.1^{+0.2}_{-0.4}$								
$M_{^{56}\mathrm{Ni}}$ $[M_\odot]$	0.50(2)	≈ 0.7	0.49(9)						
$M_{^{57}\mathrm{Co}}$ $[M_\odot]$	0.012(2)								
Mn/Fe						$0.025^{+0.008}_{-0.007}$	$0.010^{+0.007}_{-0.0035}$	$0.013^{+0.007}_{-0.005}$	0.0084(10)
Ni/Fe						$0.17^{+0.07}_{-0.05}$	$0.045^{+0.03}_{-0.015}$	$0.025^{+0.015}_{-0.01}$	0.054(7)

NOTE—[1] Shappee et al. (2017); [2] Graur et al. (2016); [3] Diehl et al. (2015); [4] Yang et al. (2018); [5] Graur et al. (2018); [6] Jacobson-Galán et al. (2018); [7] Yamaguchi et al. (2015); [8] Asplund et al. (2009)

mated $^{57}\mathrm{Co}/^{56}\mathrm{Ni} = 0.066^{+0.009}_{-0.008}$, which is higher than the other objects. On the other hand, (Graur et al. 2018) observed light curves of SN 2015F to 1040 days and estimated $^{57}\mathrm{Co}/^{56}\mathrm{Ni} = 0.004^{+0.003}_{-0.002}$, which is significantly lower than the others. Jacobson-Galán et al. (2018) observed light curves of SN 2013aa to 1500 days and reported $^{57}\mathrm{Co}/^{56}\mathrm{Ni} = 0.02^{+0.01}_{-0.02}$, although this result is consistent with zero.

2.2. *SNIa Remnants*

Observations of characteristic X-ray recombination lines in supernova remnants allow constraints on the production of new nuclei in supernovae, even though one must correct for the fact that some of the radiating material will be swept up from the surrounding gas. Yamaguchi et al. (2015) analysed the Type Ia supernova remnant (SNR) 3C 397 with archival data of the Suzaku X-ray mission. From the observed K-shell emission lines they inferred an excess in Ni and Mn production with respect to Fe, with $\mathrm{Ni/Fe} = 0.17^{+0.07}_{-0.05}$ and $\mathrm{Mn/Fe} = 0.025^{+0.008}_{-0.0077}$. This is indicative that burning at higher density may have occurred in this explosion, suggesting a Chandrasekhar-mass explosion.

2.3. *Mass of ^{56}Ni*

It is common practice to estimate the ^{56}Ni mass produced in SNIa explosions through Arnett's rule, i.e. one interprets the brightness at maximum light in terms of the radioactive input from ^{56}Ni decay. For the first time, however, Diehl et al. (2015) directly detected and traced the brightness of the characteristic γ-ray lines at 847 and 1238 keV from the β-decay chain of ^{56}Ni in SN 2014J. Comparing light curves for a variety of 1D models, they derived a ^{56}Ni mass of $(0.49 \pm 0.09) M_\odot$. The quoted uncertainty includes the range of model dependence, as models must be used to interpret the characteristic brightness evolution of the gamma-ray emission at the time the supernova gradually leaks out these gamma rays.

From a similar analysis of the same INTEGRAL data, Churazov et al. (2015) inferred a Ni mass constraint of 0.54-.67 $M_\odot$, using a different set of models for the gamma-ray light curve, and fixing the poorly constrained ejecta mass to 1.4 $M_\odot$. Obviously, even for such rather direct measurements, model dependencies still contribute to the uncertainties. Nevertheless, the ^{56}Ni mass estimate is consistent with those deduced from Arnett's rule and optical data, and also the ^{56}Ni production in SN 2011fe estimated by Shappee et al. (2017). We choose the value and uncertainties of $(0.49 \pm 0.09) M_\odot$ for our analysis here.

2.4. *Solar abundances*

The abundances of elements in solar material also provide an observational constraint, as nucleosynthesis in AGB and massive stars and their core collapse supernovae have been shown not to produce Mn in excess of the solar ratios (Nomoto, Kobayashi, & Tominaga

2013). Seitenzahl et al. (2013b) and Kobayashi, Nomoto, & Hachisu (2015) compared the Mn production of various SNIa models with the solar Mn/Fe ratio. The Mn production is sensitive to the progenitor mass (near-Chandra or sub-Chandra) and only near-Chandra models predict [Mn/Fe] > 0. They concluded that [Mn/Fe] in the solar system cannot be reproduced without near-Chandra models, while the best fit is for equal portions of near-Chandra and sub-Chandra models. We independently deduce a similar conclusion here based upon the observed nucleosynthesis.

3. EXPLOSION MODELS

The various explosion models considered in the present work are summarized in Table 2. These span the gamut of symmetry from spherical to 3D and from Chandra to sub-Chandra environments. Among these models, in the present work we have explicitly re-evaluated the nucleosynthesis of two explosion models in a post-processing network. Trajectories from the W7 deflagration (Nomoto, Thielemann, & Yokoi 1984; Thielemann, Nomoto, & Yokoi 1986) and the WDD2 delayed detonation models (Iwamoto et al. 1999) were re-evaluated in an updated nucleosynthesis network. Nucleosynthesis results were then compared to those from other explosion models and to observations of SNe Ia light-curve data and remnants.

The W7 deflagration model is a 1D flame propagation model. The explosion is postulated to result in an increase of nuclear burning due to an increase in the surface area of the flame front as it propagates outward toward the surface of the white dwarf. In this explosion mechanism, the speed of the flame is derived from mixing-length theory. In the W7 model (Nomoto, Thielemann, & Yokoi 1984), the flame accelerates to $0.08c_s$ after 0.6 s and to $0.3c_s$ after 1.18 s (where c_s is the local sound speed).

In the case of the WDD2 delayed detonation model (Iwamoto et al. 1999), the explosion begins as a spherical deflagration and transitions to a detonation at a low density (Khokhlov 1991) with the transition density given as a parameter of the model. In the model studied here, the deflagration phase was taken from the description and parametrisation of Nomoto, Thielemann, & Yokoi (1984) and was followed by the detonation phase taken from the numerical results given by Iwamoto et al. (1999) with a transition density at 2.2×10^7 gcm^{-2}. In the present work, the nucleosynthesis was recalculated for the spherically symmetric trajectories of the WDD2 model.

To evaluate the differences in nucleosynthesis in each explosion, we ran a nuclear reaction network (Meyer & Adams 2007) decoupled from the explosion model using individual trajectories from each explosion as input to the network. Each trajectory was obtained as a sequence of burning at time, t, in a particular mass range. At each time step, the electron chemical potential and electron fraction Y_e were computed implicitly for the determination of the electron capture (EC) rates. The reaction network used the EC rates computed from the GXP shell model (Honma et al. (2004), Honma et al. (2005), Suzuki et al. (2011)) for the pf-shell nuclei with $21\leq Z \leq 32$ and mass A, $42 \leq A \leq 71$. These rates have been updated from those used in Mori et al. (2016) by extending the region of pf-shell nuclei from $45 \leq A \leq 65$ as well as including the back-resonance contributions (Langanke & Martínez-Pinedo 2001). They are given for densities $\rho Y_e = 10^5 \sim 10^{11}$ g/cm^3 and temperatures $T_9 = 10^{-2} \sim 10^2$ with $T = T_9 \times 10^9$ K (Honma & Suzuki 2017). The rates of Oda et al. (1994) were used for sd-shell nuclei and the rates of Fuller, Fowler, & Newman (1982a,b) were used for the remaining rates. Rates for all other reactions were taken from the JINA REACLIB V2.2 database (Cyburt et al. 2010).

Some differences in the nuclear yields are obtained for ^{65}Cu in the W7 model. Apparent changes in the mass fractions (Table 3) of the neutron-rich Ca and Zn isotopes are minor and insignificant. The abundance of ^{41}K is enhanced by 2-3 orders of magnitude compared to Mori et al. (2016) in both the W7 and the WDD2 model. This reflects the proper inclusion of the β decay of ^{41}Ca to ^{41}K in this paper. Therefore, the values reported here supersede those previously reported in (Mori et al. 2016).

We point out that our approach of post-processing does not account for the second-order effect of the different amount of heating from differences in the nuclear rates. This limitation of decoupling the reaction network from the explosion trajectories, however, allows for a rapid evaluation of the nucleosynthesis. These approximations and their impact have been discussed in prior work (Mori et al. 2016).

A comparison of the observed nucleosynthesis (cf. Table 1) to the calculated yields among different models (cf. Table 2) can provide insight into the explosion mechanism of SNIa. The results of our new spherical network calculations are compared with the results of the cylindrically symmetric delayed detonation and deflagration models of Leung & Nomoto (2018) as well as the 3D (N100) delayed detonation model of Seitenzahl et al. (2013a), the 3D (N150def) deflagration model of Fink et al. (2014), and the violent merger model of Pakmor et al. (2012). Among these, the N100 model is a three dimensional non-rotating, delayed detonation model with an initial central density of 2.9×10^9 g/cm^3, a mass of 1.4M$_\odot$, and an initial radius of 1.96×10^8 cm. The N150def model is a 3D model for a deflagration scenario.

Both of the 3D models were run with the same hydrodynamics codes. The details of the computational methods are described in their respective references. The violent merger model is a 3D simulation of two sub-Chandrasekhar mass WDs. Our comparison among the W7, WDD2, LN18(def.), LN18(del. det.), N100, N150def, and violent merger model can shed light on the viability of each explosion model and effects of modeling in spherical, cylindrical, or unconstrained symmetry.

4. RESULTS DISCUSSION

4.1. *Comparisons among models*

The final isotopic abundance profiles for the updated W7 and WDD2 models computed in this work are shown in Figure 1 as a function of ejected mass for the inner 0.1 M$_\odot$ of the ejecta. The resulting mass fractions closely resemble those of prior work (Brachwitz et al. 2000).

In addition to the isotopic abundance profiles, the total overproduction factors for the W7 and WDD2 explosion models are shown in Figure 2. This is defined by the ratio of an isotopic species i relative to iron, normalized to the same ratio in the solar abundance standard:

$$\frac{Y_i/Y_{Fe}}{Y_{i,\odot}/Y_{Fe,\odot}} = \frac{Y_i/Y_{i,\odot}}{Y_{Fe}/Y_{Fe,\odot}} \qquad (2)$$

These abundances are the total ejected abundance in an event, calculated by weighting the yield in each shell by the mass of that shell.

Both these models and their yields (evaluated with a different nuclear network) have been discussed previously (Brachwitz et al. 2000). As we discussed in a previous paper (Mori et al. 2016), the WDD2 model appears to reproduce solar distributions more closely for Cr, Mn, Fe, Ni, Cu, and Zn than the W7 model. Both of these models underproduce Cu and Zn, and show an overall trend of enhanced production of lighter nuclei within an isotopic chain, with some exceptions.

The most notable of these exceptions is Cr: In the WDD2 model, neutron-rich Cr is enhanced relative to the proton-rich species in the chain, as compared to Cr production in the W7 model. Similarly, Cr is more strongly produced

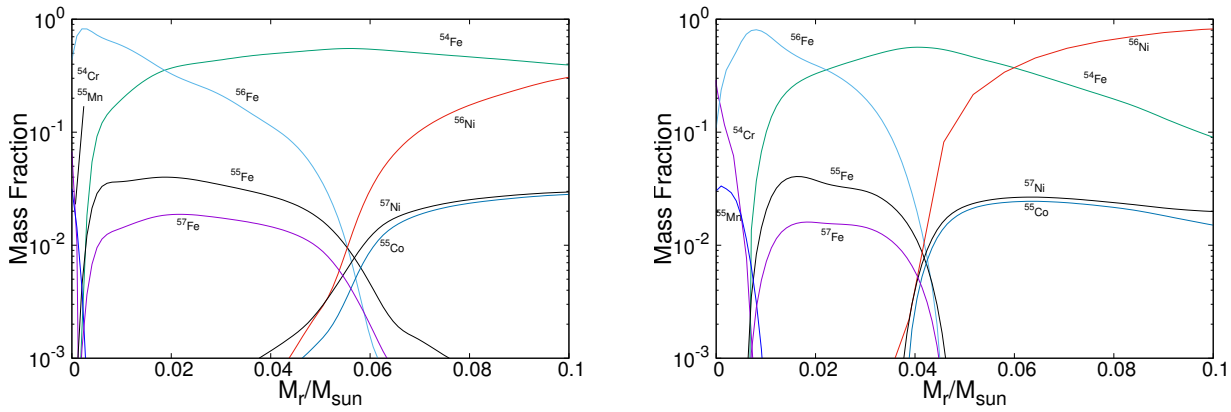

Figure 1. Abundance plots for the inner part of the W7 model (left panel) and the WDD2 model (right panel). Only nuclei which are mentioned in the text are shown.

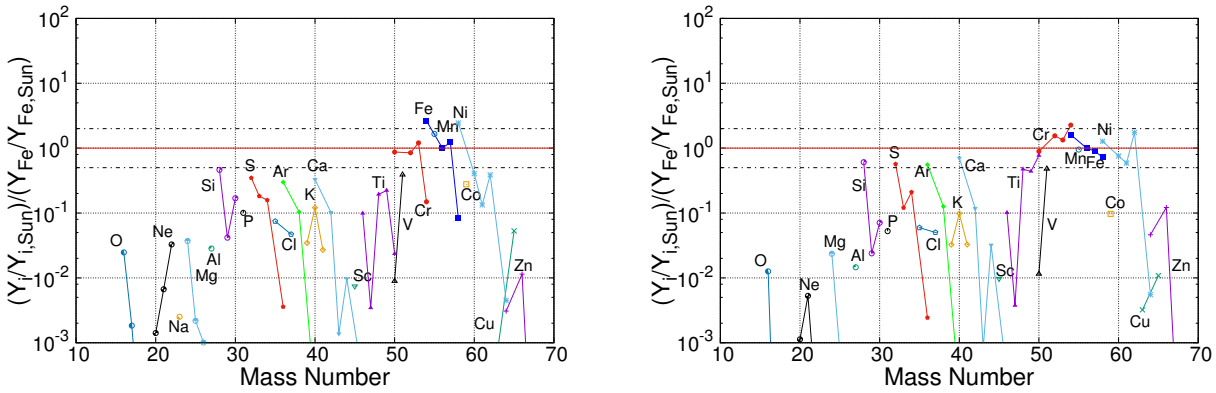

Figure 2. Abundances of nuclei produced in the W7 model (left) and the WDD2 model (right), normalized by the solar abundance and the ^{56}Fe abundance (Mori et al. 2016).

in the central trajectories of the WDD2 explosion model, as seen in Figure 1. In the central 0.01 $M_\odot$ region of the star, the WDD2 model obtains a significant mass fraction of Cr, while the W7 model predicts little Cr production. Hence, observational constraints on Cr could be a good indicator of the explosion mechanism for a SN Ia event.

A comparison of the W7 and WDD2 two models calculated in this work is summarized in Figure 3, and the yields of several isotopes for these two models are shown in Figure 3. The ratio of total mass yields for the WDD2 model to that of the W7 model is shown for various isotopic chains. For elements with $20 \leq Z \leq 28$, there is a general trend towards an increased production of neutron-rich nuclei (higher Y_e) in the WDD2 model. The ratio of ^{54}Cr is also noted as this is produced in reasonable abundance in the WDD2 model, but significantly less in the W7 model.

Model results for various isotopic and elemental ratios are summarized in Table 2. These include the total mass fraction ratios ^{57}Co/^{56}Ni and ^{55}Fe/^{57}Co as well as the total computed ejected mass of ^{56}Ni, ^{57}Co, ^{54}Cr, and ^{54}Fe. In addition, the ratios of the total elemental mass of Mn/Fe and Ni/Fe are given.

The total mass of ^{56}Ni ejected agrees within about 10% for all models, except for the deflagration models LN18(def.) and N150def models, which predict a much lower yield. For ^{57}Co, the W7, the LN18(del.det.) and the N100 models appear to predict similar values, while the

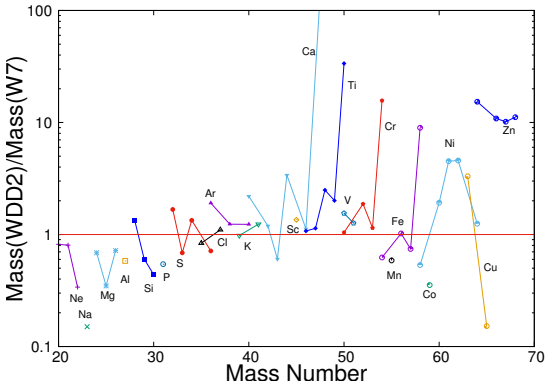

Figure 3. Ratio of the ejected mass of nuclei produced in the WDD2 model to the mass of those produced in the W7 model (Mori et al. 2016).

other models predict about 30% less. The ^{54}Cr yields, however, differ dramatically among the models; this is a further indication that this isotope as a good diagnostic for the explosion mechanism. To a lesser extent, the production of ^{54}Fe may constrain the explosion mechanism, as the values for similar models can vary by as much as 25% from the average value. The elemental ratios of Mn/Fe and Ni/Fe may also be used as indicators. The W7, LN18, and N100 models predict similar ratios, while the WDD2 model predicts significantly less Mn/Fe and Ni/Fe, and the N150def model predicts somewhat larger ratios for Mn/Fe and Ni/Fe.

As an estimate of the model uncertainties, we have made use of a recent broad parameter study for the LN18 SNIa models of Leung & Nomoto (2018). In that study cylindrically symmetric 2D models were run for a wide range of central masses and composition, along with different flame ignition and propagation treatments. We use this broad study as a reference with fixed solar metallicity, and assume that the other models have the same order of uncertainty of their yields. That is, for each of the diagnostic ratios of interest here we take the extreme values from the range of models considered in Leung & Nomoto (2018) as an estimate of the range of uncertainty in the computed results. We note however that the Leung & Nomoto (2018) models are Chandra deflagration and delayed-detonation models. As such they have discussed uncertainties related to for example the flame propagation, DDT, or ignition setup and density. However, the violent merger model does not share any of these uncertainties, as it consists chiefly of a detonation, with composition and mass of the primary as the most important parameters. Hence, we do not draw error bars for the violent merger model.

This range of model uncertainty is illustrated in Figure 4 where we compare the ejected mass ratios of of ^{57}Co/^{56}Ni, ^{55}Fe/^{56}Ni, ^{54}Cr/^{56}Ni, and ^{54}Fe/^{56}Ni as a function of the WD central density. The green bands show the range of results of the delayed-detonation models in LN18. So, for example the uncertainty in the ^{57}Co/^{56}Ni ratio is taken from the highest and lowest ratio in the corresponding green band in the upper left panel of Fig. 4. This logarithmic range of uncertainty was then adopted for all of the models surveyed here.

Regarding Figure 4, there are a number of trends worthy of note. For one, The density dependence of ^{57}Co production is not very strong in the cyrindrically symmetric models of LN18, while there appears to be a positive correlation when going from the low density spherical W7 and WDD2 models to the 3D N100 and N150 models. For both ^{55}Fe and ^{54}Fe production, all models show such a correlation with density. Therefore the nucleosynthesis of ^{55}Fe and ^{54}Fe may be used as an diagnostic of the density of the progenitor.

The production of ^{54}Cr is particularly interesting. Its yield spans five orders of magnitude, making its yield the most sensitive correlation with central density. The LN18 models show a strong positive correlation with density, while in other models the correlation may even be negative. We hypothesize that this may reflect the degree of symmetry of the models as indicated

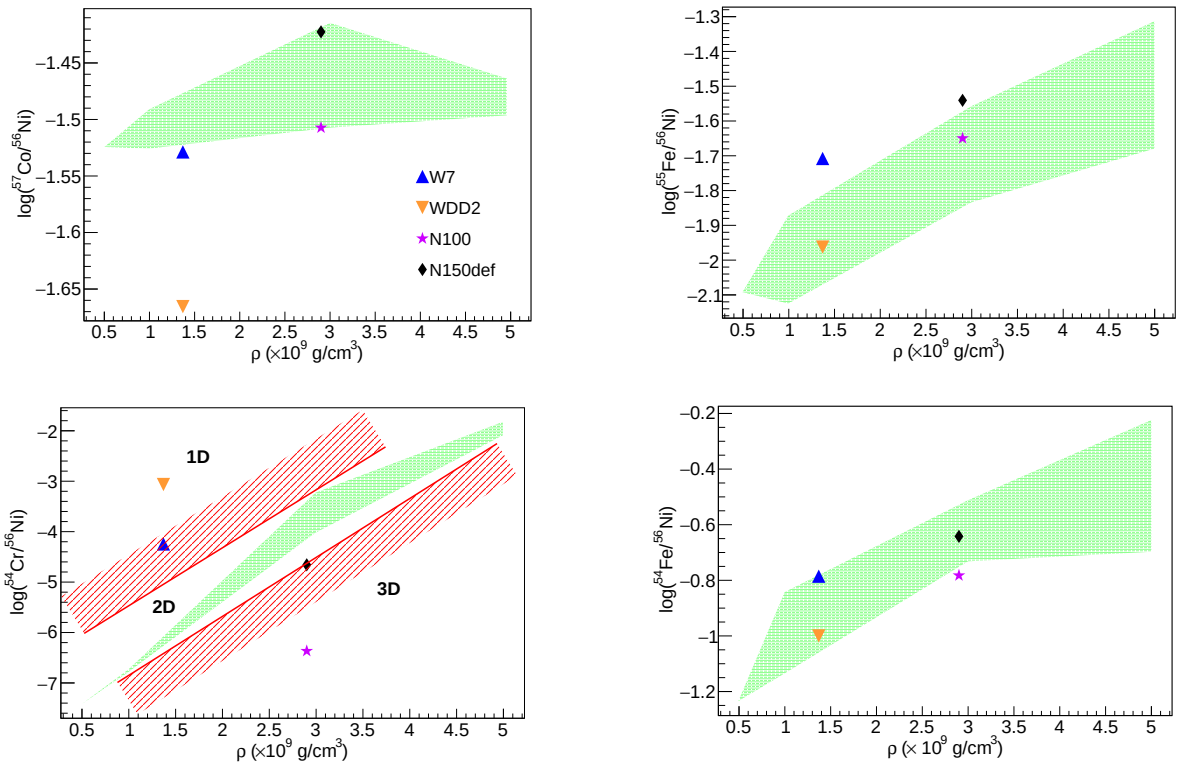

Figure 4. The ejected mass in the models normalized by the ^{56}Ni mass. The green regions show the results of LN18. The red regions in the ^{54}Cr case show expected density dependence for spherical and three dimensional models.

by the schematic red bands in the corresponding lower left panel of Fig. 4. The spherical W7 and WDD2 models have a higher ^{54}Cr production, while the three dimensional models have a lower production. We emphasize, however, that the tendency for one and three dimensional models (as shown by the red regions in this figure) may be indicative, but clearly need to be substantiated with more simulations.

We also note the differences between the deflagration and delayed-detonation models on this figure. More ^{54}Cr (with a $Y_e = 0.44$) is produced in WDD2 than in the W7 model. However, the order is opposite for the production of ^{54}Fe (with $Y_e = 0.48$). Because each model is characterized by a different final Y_e, a reversal in production is perhaps expected, but this reversal is not as pronounced when comparing ^{56}Ni ($Y_e = 0.5$) and ^{57}Co ($Y_e = 0.47$). This indicates a lower Y_e in the WDD2 model than in the W7 model.

However, this trend is reversed for the 3D explosion calculations. Given the results of Figure 4, switching from the delayed detonation model to the deflagration model results in a lower abundance of ^{54}Fe, but higher abundance of ^{54}Cr. In the case of 3D models, the deflagration model appears to result in a lower value for Y_e as compared to the delayed detonation model.

Nevertheless, there are some interesting trends among the models summarized in Table 2. Overall the sub-Chandra double-degenerate scenarios such as the violent merger model predict lower values for the ^{57}Co/^{56}Ni and ^{55}Fe/^{57}Co ratios, while the deflagration and Chandra single degenerate scenarios like the 2D LN18 models and the 3D N100 and N150def models predict higher ratios.

A similar trend occurs in the Mn/Fe and Ni/Fe yields, i.e. that the sub-Chandra models predict a low Mn/Fe ratio while the Chandra deflagration models like N150def predict the highest ratio. These trends are compared with observations in the next section to possibly diagnose the nature of each observed SNIa explosion.

4.2. *Comparison to observations*

In Figures 5 and 6, we compare models to observations using the above elemental and isotopic yields as criteria.

4.2.1. *Comparison to light-curve data*

Figure 5 in particular shows observational results deduced from direct light-curve SNIa photometry. Observational data are shown as thick data points and error bars, while the thin data points with error bars are the yields of the theoretical models as labeled. As described in the previous section we indicate uncertainty in the model results through 'error bars', which should reflect the variation of yields due to the parameters of each model.

The left panel of Figure 5 shows the ratios of ^{57}Co to ^{56}Ni for the models from Table 2 compared to observations of SN 2011fe, 2012cg, 2014J, 2015F, and 2013aa. The two events SN 2011fe and SN 2012cg compare well with the model predictions and suggest different explosion scenarios.

The predictions from the violent merger calculation and the spherical delayed detonation (WDD2) model are most consistent with observations of SN 2011fe, while the predictions from the 3D deflagration model are most consistent with observations of SN 2012cg. In both the 3D and 1D models, the production of ^{57}Co relative to ^{56}Ni is higher in the deflagration model than in the delayed detonation model. The cylindrically symmetric models of LN fall in between and appear consistent with both events.

Recently, late light-curves of SN 2014J (Yang et al. 2018), 2015F (Graur et al. 2018), and 2013aa (Jacobson-Galán et al. 2018) have been measured and the ^{57}Co/^{56}Ni ratios were estimated (Figure 5). The result for SN 2013aa is just an upper limit but consistent with all of the models. The other two objects, however, cannot be explained by any of them. These results are subject to systematic uncertainties, so future observations are desireble to understand these events.

The right side of Figure 5 shows the observed ratio of ^{55}Fe to ^{57}Co for SN 2011fe. All models produce somewhat higher ratios [i.e. $\log_{10}(^{55}\mathrm{Fe}/^{57}\mathrm{Co}) \sim -0.2$] than that deduced from observation, although the violent merger model comes closest, within uncertainties. The lower density associated with sub-$M_{\rm ch}$ models including the violent merger apparently results in this lower ^{55}Fe/^{57}Co ratio.

Based upon this figure we would identify SN 2011fe as most likely being a sub-Chandra violent merger event, while SN 2012cg appears to be best fit with the higher-density single-degenerate Chandra deflagration models, particularly the highest-density N150def 3D model.

In Figure 6 we show the correlation from supernova remnant spectroscopy of the mass ratios of [Mn/Fe] and [Ni/Fe]. Three SN remnants, 3C 397, Kepler, and Tycho, are compared to the computational results from Table 4. Since no result for the [Ni/Fe] value is given from the violent merger model, the [Ni/Fe] value for this model is shown with a large horizontal error bar in the figure. It is difficult to estimate uncertainties of [Mn/Fe] for the violent merger model, but any set of parameters in sub-Chandra models produces [Mn/Fe]< 0 (Seitenzahl et al. 2013b).

Although with only three remnants the number of observations is small, [Mn/Fe] appears slightly above solar in all remnants. The dashed circles in this figure identify two approximate

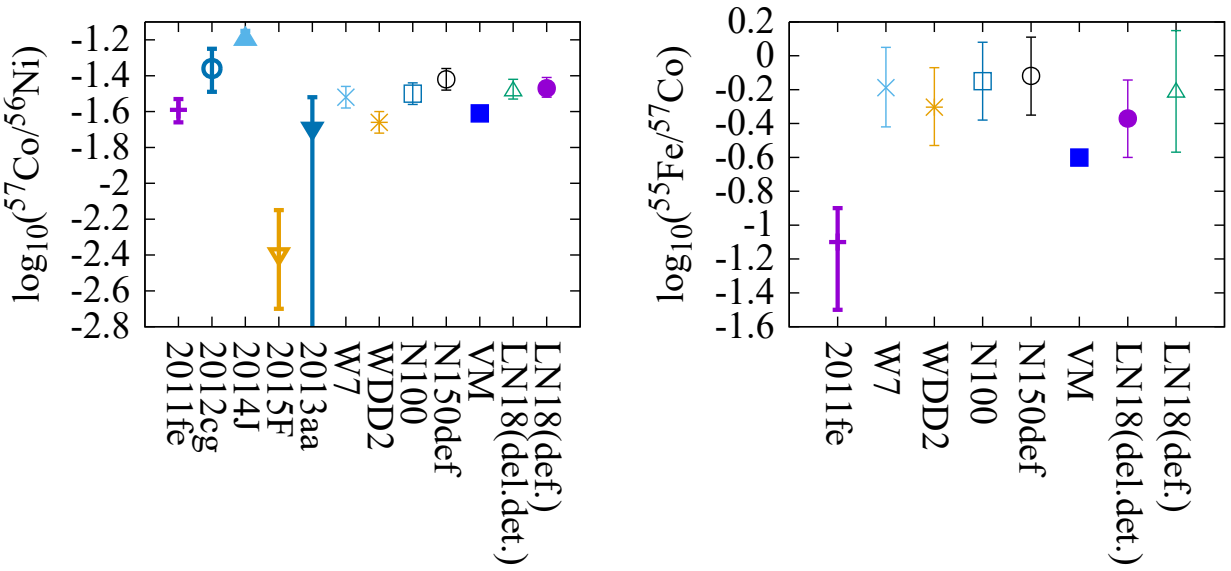

Figure 5. Ratios of the ejected mass. The thick points are the observational data and the thin points are the models. The variability of the delayed-detonation model results with model parameter variation as reported in Leung & Nomoto (2018) (referred to as LN18 in the figure) is used as a guidance to the uncertainty of the theoretical model results.

groupings of the models. The remnant 3C 397 shows much higher Mn and Ni relative to Fe and matches well the Chandra 3D N150def model. The Tycho event, however, is not explained by any of the shown models. It is difficult to draw definitive conclusions on Kepler, but it is notable that Tycho and Kepler coincide with each other within the error bars. Therefore, they may originate from similar progenitors.

Considering the uncertainties in the models, it is somewhat speculative to attempt to specify the explosion mechanisms of these events. Nevertheless, the difference between the 3C 397 and the overlapping results from the Kepler and Tycho supernova remnants may imply that both explosion mechanisms occur, i.e. a Chandra single-degenerate explosion higher-density model for 3C 397 vs. a sub-Chandra lower-density event for the Tycho and Kepler remnants.

With only one stable isotope ($A = 55$) produced by the decay of ^{55}Fe, the production of Mn may be more sensitive to the Y_e in the explosion. The lower Y_e of the deflagration model may result in a higher yield of Mn. However, neither does the spherical deflagration model predict a convincingly-higher Mn yield, nor does the 3D delayed detonation model predict the lower [Mn/Fe] and [Ni/Fe] values.

It is possible that continued spectral observations of supernova remnants can confirm this trend of the explosion mechanisms of various progenitors. In particular, further observations of SNe Ia remnants may add data for Mn and Ni with values in between those for the Kepler and 3C 397 remnants or that continue this trend of clumping around the sub-Chandra and Chandra models.

5. CONCLUSIONS

In this work, we have computed new revised nucleosynthesis yields based upon new EC rates. We also made a new summary of the nucleosynthesis yields in several recently analysed light curves. We have compared the results of various spherical, cylindrical, and 3D SNe Ia explosion models in both single-degenerate Chandra models and double-degenerate sub-Chandra environments. Simulations included deflagration and deflagration-plus-delayed-detonation

Table 2. Summary of Explosion Models.*

Model	W7[1]	WDD2[1]	LN18 (del.det.)[6]	LN18 (def.)[6]	N100[3]	N150def[4]	VM[2,5]
Dimension	1	1	2	2	3	3	3
Mechanism**	Def.	Del. Det.	Del. Det.	Def.	Del. Det.	Def.	Double Degen. Sub-Chandra
$\log_{10}(^{57}\mathrm{Co}/^{56}\mathrm{Ni})$	−1.52	−1.66	-1.48	-1.47	−1.50	−1.42	−1.61
$\log_{10}(^{55}\mathrm{Fe}/^{57}\mathrm{Co})$	−0.188	−0.303	-0.37	-0.21	−0.150	−0.120	−0.601
$M_{^{56}\mathrm{Ni}}$ $[M_\odot]$	0.651	0.668	0.530	0.300	0.604	0.378	0.616
$M_{^{57}\mathrm{Co}}$ $[M_\odot]$	0.0193	0.0144	0.0171	0.0106	0.0188	0.0143	0.0149
$M_{^{54}\mathrm{Cr}}$ $[M_\odot]$	3.71×10^{-5}	5.77×10^{-4}	2.40×10^{-3}	2.42×10^{-3}	2.61×10^{-7}	8.28×10^{-6}	
$M_{^{54}\mathrm{Fe}}$ $[M_\odot]$	0.107	0.0670	0.107	0.101	0.0994	0.0862	
Mn/Fe	0.0158	0.00964	0.0127	0.0160	0.0125	0.0219	0.00594
Ni/Fe	0.0916	0.0635	0.0960	0.102	0.0999	0.138	

NOTE—[1] Mori et al. (2016); [2] Röpke et al. (2012); [3] Seitenzahl et al. (2013a); [4] Fink et al. (2014); [5] Seitenzahl et al. (2013b); [6]Leung & Nomoto (2018)

NOTE—*Results from the violent merger model do not report ^{54}Cr or ^{54}Fe yields.

NOTE—** "Def" or "Del. Det." mean a deflagration model or a delayed-detonation Chandra model, respectively.

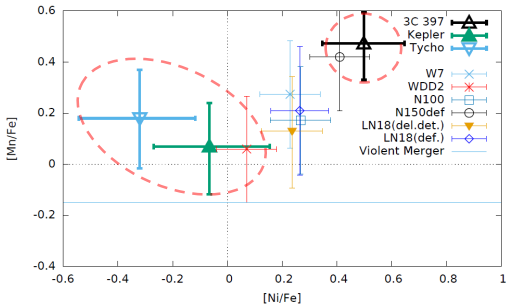

Figure 6. Observational data of SNRs and theoretical results of SN Ia models. Dashed-oval regions are drawn to aid in identifying the groupings of data and models. The thick points are the observational data and the thin points are the models. The variability of the delayed-detonation model results with model parameter as reported in Leung & Nomoto (2018) is used as a guidance to uncertainty of the theoretical model results.

explosions, and a 3D violent merger model. Isotopic and elemental yields for several key species were summarized for these models (Table 2). Elemental and isotopic ratios from these models were also compared to quantities inferred from SNIa light curves and remnant observations. For our comparisons, we attempt to include uncertainties in models from different parameter choices by adopting range of results from a recent broad parameter study with cylindrically symmetric models (Leung & Nomoto 2018).

While no explosion model was able to reproduce the constraints of all of the observations, some models appear slightly better at reproducing different observational constraints simultaneously. In particular, we find that the models and the observed nucleosynthesis tend divide nearly equally into two groups roughly characterized by the central densities during thermonuclear burning. One set of observations (including SN2011fe and the Kepler and Tycho remnants) is consistent with the low central densities of sub-Chandra double-degenerate merger models, while the other set (including SN2012cg and the 3C 397 remnant) favors the higher central densities of single-degenerate Chandra models.

We note that observations of ^{54}Cr and ^{54}Fe would be good diagnostics of the explosion model: ^{54}Cr is only produced in a significant abundance in the center of the WDD2 model. And the relative amounts of ^{54}Cr and ^{54}Fe apparently vary systematically with both the explosion models (deflagration or delayed-detonation) and the deviation from spherical

Table 3. Mass fractions for the nuclei produced in the W7 and WDD2 model. The underlined nuclei are produced in one model by more than twice as much as in the other model. The dashed-underlined nuclei are produced in the models at a level of less than $10^{-5} M_\odot$.

	W7 [$M_\odot$]	WDD2 [$M_\odot$]		W7 [$M_\odot$]	WDD2 [$M_\odot$]
^{12}C	4.794×10^{-2}	1.359×10^{-3}	^{45}Sc	1.639×10^{-7}	2.217×10^{-7}
^{13}C	4.150×10^{-8}	3.292×10^{-8}	^{46}Ti	1.225×10^{-5}	1.321×10^{-5}
^{14}N	5.809×10^{-6}	3.308×10^{-8}	^{47}Ti	4.021×10^{-7}	4.565×10^{-7}
^{15}N	2.100×10^{-8}	5.473×10^{-10}	^{48}Ti	2.385×10^{-4}	5.959×10^{-4}
^{16}O	1.356×10^{-1}	7.061×10^{-2}	^{49}Ti	2.085×10^{-5}	4.195×10^{-5}
^{17}O	4.084×10^{-6}	6.553×10^{-9}	^{50}Ti	2.184×10^{-6}	7.329×10^{-5}
^{18}O	6.441×10^{-8}	1.606×10^{-10}	^{50}V	4.721×10^{-9}	6.220×10^{-9}
^{19}F	5.056×10^{-10}	4.061×10^{-12}	^{51}V	8.376×10^{-5}	1.057×10^{-4}
^{20}Ne	1.309×10^{-3}	1.072×10^{-3}	^{50}Cr	3.710×10^{-4}	3.868×10^{-4}
^{21}Ne	1.576×10^{-6}	1.274×10^{-6}	^{52}Cr	7.209×10^{-3}	1.347×10^{-2}
^{22}Ne	2.442×10^{-3}	8.267×10^{-4}	^{53}Cr	1.184×10^{-3}	1.345×10^{-3}
^{23}Na	4.801×10^{-5}	7.138×10^{-6}	^{54}Cr	3.660×10^{-5}	5.737×10^{-4}
^{24}Mg	1.026×10^{-2}	7.081×10^{-3}	^{55}Mn	1.259×10^{-2}	7.391×10^{-3}
^{25}Mg	8.447×10^{-5}	2.943×10^{-5}	^{54}Fe	1.077×10^{-1}	6.706×10^{-2}
^{26}Mg	4.478×10^{-5}	3.215×10^{-5}	^{56}Fe	6.683×10^{-1}	6.834×10^{-1}
^{27}Al	8.509×10^{-4}	4.946×10^{-4}	^{57}Fe	2.018×10^{-2}	1.503×10^{-2}
^{28}Si	1.732×10^{-1}	2.321×10^{-1}	^{58}Fe	1.741×10^{-4}	1.556×10^{-3}
^{29}Si	7.921×10^{-4}	4.786×10^{-4}	^{59}Co	5.368×10^{-4}	1.905×10^{-4}
^{30}Si	2.215×10^{-3}	9.728×10^{-4}	^{58}Ni	6.936×10^{-2}	3.694×10^{-2}
^{31}P	4.602×10^{-4}	2.503×10^{-4}	^{60}Ni	4.523×10^{-3}	8.690×10^{-3}
^{32}S	7.890×10^{-2}	1.317×10^{-1}	^{61}Ni	6.557×10^{-5}	2.960×10^{-4}
^{33}S	3.312×10^{-4}	2.272×10^{-4}	^{62}Ni	6.165×10^{-4}	2.824×10^{-3}
^{34}S	1.712×10^{-3}	2.291×10^{-3}	^{64}Ni	1.863×10^{-6}	2.322×10^{-6}
^{36}S	1.878×10^{-7}	1.336×10^{-7}	^{63}Cu	2.499×10^{-7}	1.082×10^{-6}
^{35}Cl	1.045×10^{-4}	8.783×10^{-5}	^{65}Cu	2.381×10^{-7}	3.616×10^{-8}
^{37}Cl	2.280×10^{-5}	2.510×10^{-5}	^{64}Zn	1.749×10^{-6}	2.680×10^{-5}
^{36}Ar	1.324×10^{-2}	2.519×10^{-2}	^{66}Zn	3.848×10^{-6}	4.184×10^{-5}
^{38}Ar	9.140×10^{-4}	1.132×10^{-3}	^{67}Zn	2.445×10^{-9}	2.478×10^{-8}
^{40}Ar	2.074×10^{-9}	2.546×10^{-9}	^{68}Zn	1.313×10^{-9}	1.458×10^{-8}
^{39}K	6.752×10^{-5}	6.611×10^{-5}			
^{41}K	4.068×10^{-6}	5.026×10^{-6}			
^{40}Ca	1.133×10^{-2}	2.477×10^{-2}			
^{42}Ca	2.428×10^{-5}	2.901×10^{-5}			
^{43}Ca	7.151×10^{-8}	4.318×10^{-8}			
^{44}Ca	7.907×10^{-6}	2.675×10^{-5}			
^{46}Ca	4.357×10^{-10}	4.885×10^{-10}			
^{48}Ca	2.778×10^{-13}	1.965×10^{-10}			

symmetry of the explosion model. A dependence on symmetry may come from the fact that spherically symmetric models tend to overestimate the degree of neutronization because of the suppressed buoyancy degrees of freedom.

Clearly there is a need for more observational elemental and isotopic ratios. Only in this way can observations be tested for consistency with model predictions in all aspects of predicted light-curve shapes, elemental ratios around the iron group, and isotopic yields which are sensitive to the electron fraction and density of the burning regions. However, a preliminary conclusion of the present study is a tendency

for the observations to equally cluster around either the Chandra or sub-Chandra model results, suggesting that both models contribute substantially to observed SNIa events.

In this study, we used nucleosynthetic results from six Chandra models, while only the violent merger model is included as a sub-Chandra model. This is because detailed nucleosynthetic yields are calculated and published only for few sub-Chandra models. It is desirble that extended studies on nucleosynthesis in sub-Chandra models with large reaction networks be performed in the future.

KM's work was supported by NSF grant PHY-1430152; MAF's by NSF grant PHY-1204486 and by an NAOJ Visiting Research Professorship; TK's by JSPS KAKENHI Grant Numbers JP15H03665 and JP17K05459; KN's and S.C.L.'s by the World Premier International Research Center Initiative (WPI), MEXT, Japan, and by JSPS KAKENHI Grant Numbers JP26400222, JP16H02168, and JP17K05382; and TS's was supported in part by JSPS KAKENHI Grant number JP15K05090. The work of GJM is supported in part by the U.S. Department of Energy through Nuclear Theory Grant DE-FG02-95-ER40934.

REFERENCES

Arnett, D. 1996, *Supernovae and Nucleosynthesis: An Investigation of the History of Matter from the Big Bang to the Present*, Princeton: Princeton University Press

Arnett, W.D. 1979, ApJ, 230, L37

Arnett, D., & Livne, E. 1994, ApJ, 427, 315

Asplund, M., Grevesse, N., Sauval, A.J., & Scott, P. 2009, ARA&A, 47, 481.

Benvenuto, O.G., Panei, J.A., Nomoto, K., Kitamura, H., & Hachisu, I. 2015, ApJL, 809, L6.

Blinnikov, S.I., & Khokhlov, A.M. 1986, Sov. Astron. Lett., 12, 131

Boyd, R.N. 2008, *An Introduction to Nuclear Astrophysics*, Chicago: The University of Chicago Press

Brachwitz, F., Dean, D.J., Hix, W.R., Iwamoto, K., Langanke, K., Martínez-Pinedo, G., Nomoto, K., Strayer, M.R., Thielemann, F.-K., & Umeda, H. 2000, ApJ 536,934

Churazov E., et al. 2015, ApJ, 812, 62

Cyburt, R.H., Amthor, A.M., Ferguson, R., Meisel, Z., Smith, K., Warren, S., Heger, A., Hoffman, R.D., Rauscher, T., & Sakharuk, A. 2010, ApJS 189, 1

Diehl, R., Siegert, T., Hillebrandt, W., Krause, M., Greiner, J., Maeda, K., Röpke, F.K., Sim, S.A., Wang, W., & Zhang, X. 2015, A&A, 574, A72

Dimitriadis, G., Sullivan, M., Kerzendorf, W., Ruiter, A. J., Seitenzahl, I. R., Taubenberger, S., Doran, G. B., Gal-Yam, A., Laher, R. R., Maguire, K., Nugent, P., Ofek, E. O., & Surace, J. 2017 MNRAS, 468, 3798

Fink, M., Kromer, M., Seitenzahl, I.R., Ciaraldi-Schoolmann, F., Rp̈ke, F.K., Sim, S.A., Pakmor, R., Ruiter, A.J., & Hillebrandt, W. 2014, MNRAS, 438, 1762

Fransson, C., Jerkstrand, A. 2015, ApJL, 814, L2

Fransson C., Kozma C. 2002. New Astron. Rev. 46, 487

Fuller, G.M., Fowler, W.A., & Newman, M.J. 1982, ApJ 252, 715

Fuller, G.M., Fowler, W.A., & Newman, M.J. 1982, ApJS 48, 279

Gamezo, V.N., Khokhlov, A.M., & Oran, E.S. 2005, ApJ623, 337

Graur, O., Zurek, D., Shara, M.M. et al. 2016, ApJ, 819, 31

Graur, O., Zurek, D. R., Rest, A., Seitenzahl, I. R., Shappee, B. J., Fisher, R., Guillochon, J., Shara, M. M., & Riess, A. G. 2018, ApJ, 859, 79

Hillebrandt, W. & Niemeyer, J.C. 2000, ARA&A, 38, 191

Höflich, P. et al. 2017, arXiv:1707.05350

Honma, M., Otsuka, T., Brown, B.A., & Mizusaki, T. 2004, Phys. Rev. C 69, 034335

Honma, M., Otsuka, T., Mizusaki, T, Hjorth-Jensen, M, & Brown, B.A. 2005, J. Phys. Conf. Ser., 20, 7

Honma, M. & Suzuki, T. 2017, http://www.phys.chs.nihon-u.ac.jp/suzuki/data4/link.html
Hoyle,F. & Fowler, W.A. 1960, ApJ, 132, 565
Iben, I.I. & Tutukov, A.V. 1984, ApJ, 284, 719
Illiadis, C. 2008, *Nuclear Physics of Stars*, John Wiley & Sons, Inc.
Iwamoto, K., Brachwitz, F., Nomoto, K., Kishimoto, N., Umeda, H., Hix, W.R., Thielemann, F.-K. 1999, ApJS, 125, 439
Jacobson-Galán, W. V., Dimitriadis, G., Foley, R. J., & Kilpatrick, C. D. 2018, ApJ, 857, 88
Kerzendorf, W. E., McCully, C., Taubenberger, S., Jerkstrand, A., Seitenzahl, I., Ruiter, A. J., Spyromilio, J., Long, K. S., Fransson, C. 2017, MNRAS, 472, 2534
Khokhlov, A.M. 1991, A&A, 245, 114
Khokhlov, A.M. 1995, ApJ, 449, 695
Kobayashi, C., Nomoto, K., & Hachisu, I. 2015, ApJL, 804, L24
Kurfess J.D., et al., 1992, ApJ, 399, L137
Langanke, K., & Martínez-Pinedo, G. 2001, At. Data Nucl. Data Tables 79, 1
Langanke, K., & Martínez-Pinedo, G. 2003, RvMP, 75, 819
Leising M. D., 2001, ApJ, 563, 185
Leung, S. -C., & Nomoto, K. 2018, ApJ, 861, 143
Maoz, D., Mannucci, F., & Nelemans, G. 2014, ARA&A, 52, 107
Marion, G. H., Brown, P. J., Vinkó, J. et al. 2016, ApJ, 820, 92
Meyer, B.S. & Adams, D.C. 2007, Meteor. and Plan. Sci. Suppl. 2007, 5215
Mori, K., Famiano, M.A., Kajino, T., Suzuki, T., Hidaka, J., Honma, M., Iwamoto, K., Nomoto, K., & Otsuka, T. 2016, ApJ, 833, 179
Müller,D., & Arnett, W.D. 1982, ApJ, 261, L109
Nomoto, K., Iwamoto, K., & Suzuki, T. 1995, Phys.Rep., 256, 173
Nomoto, K., Kamiya, Y., & Nakasato, N. 2013, in IAU Symposium 281 "Binary Paths to Type Ia Supernova Explosions", 253 (ed. R. Di Stefano et al.) arXiv:1302.3371
Nomoto, K., Kobayashi, C., & Tominaga, N. 2013, ARAA, 51, 457
Nomoto, K., Sugimoto, D., & Neo, S. 1976, Ap&SS, 39, L37
Nomoto, K., Thielemann, F.-K., & Yokoi, K. 1984, ApJ 286, 644
Oda, T., Hino, M., Muto, K., Takahara, M., & Sato, K. 1994, ADNDT 56, 231
Pakmor, R., Kromer, M., Taubenberger, S., et al. 2013, ApJ, 747, L10
Pakmor, R., Kromer, M., Taubenberger, S., et al. 2013, ApJ, 770, L8
Perlmutter, S., et al. 1999, ApJ, 517, 565
Riess, A.G., et al. 1998, AJ, 116, 1009
Röpke, F.K., Giesleler, M., Reinecke, M., Travaglio, C., & Hillebrandt, W. 2006, A&A 453, 260
Röpke, F.K., et al. 2012, ApJ 750, L19
Sato, Y., Nakasato, N., Tanikawa, A. et al. 2016, ApJ, 821, 67
Schmidt, W., Niemeyer, J.C., Hillebrandt, W., & Röpke, F.K. 2008, A&A, 450, 283
Seitenzahl, I.R., et al., 2009, MNRAS, 400, 531
Seitenzahl, I.R., et al. 2013, MNRAS, 429, 1156
Seitenzahl, I.R., Cescutti, G., Röpke, F.K., Ruiter, A.J., & Pakmor, R. 2013, A&A, 559, L5
Shappee, B. J., Piro, A. L., Stanek, K. Z., Patel, S. G., Margutti, R. A., Lipunov, V. M., & Pogge, R. W. 2018, ApJ, 855, 6
Shappee, B.J., Stanke, K.Z., Kochanek, C.S., & Garnavich, P.M. 2017, ApJ, 841, 48
Suzuki, T., Honma, M., Mao, H., Otsuka, T., & Kajino, T. 2011, Phys. Rev. C 83, 044619
Taubenberger, S., Elias-Rosa, N., Kerzendorf, W. E., et al. 2015, MNRAS, 448, L48
Thielemann, F.-K., Nomoto, K., & Yokoi, K. 1986, A&A, 158, 17
Wang, B., & Han, Z. 2012, New Astron. Rev., 56, 122
Webbink, R.F. 1984, ApJ, 277, 355
Yamaguchi, H., Badenes, C., Foster, A.R., et al. 2015, ApJL, 801, L31
Yang, Y., Wang, L., Baade, D., Brown, P. J., Cikota, A., Cracraft, M., Höflich, P. A., Maund, J. R., Patat, F., Sparks, W. B., Spyromilio, J., Stevance, H. F., Wang, X., & Wheeler, J. C. 2018, ApJ, 852, 89